

On the validity domain of maximum likelihood estimators for depth-of-field extension in single-molecule localization microscopy

OLIVIER LÉVÊQUE,^{1,*} CAROLINE KULCSÁR,¹ ANTHONY LEE,^{2,3} PIERRE BON,^{2,3} LAURENT COGNET,^{2,3} AND FRANÇOIS GOUDAIL¹

¹Université Paris-Saclay, Institut d'Optique Graduate School, CNRS, Laboratoire Charles Fabry, 91127, Palaiseau, France

²Université de Bordeaux, Laboratoire Photonique Numérique et Nanosciences, UMR 5298, 33400, Talence, France

³Institut d'Optique & CNRS, LP2N UMR 5298, 33400, Talence, France

*Corresponding author: olivier.leveque@institutoptique.fr

Received 9 August 2021; revised 6 November 2021; accepted 9 November 2021; posted 9 November 2021; published 9 December 2021

Localization microscopy approaches with enhanced depth-of-field (EDoF) are commonly optimized using the Cramér–Rao bound (CRB) as a criterion. It is widely believed that the CRB can be attained in practice by using the maximum-likelihood estimator (MLE). This is, however, an approximation, of which we define in this paper the precise domain of validity. Exploring a wide range of settings and noise levels, we show that the MLE is efficient when the signal-to-noise ratio (SNR) is such that the localization standard deviation of a single molecule is less than 20 nm. Thus, our results provide an explicit and quantitative validity boundary for the use of the MLE in EDoF localization microscopy setups optimized with the CRB. © 2021 Optical Society of America

<https://doi.org/10.1364/JOSAA.439993>

1. INTRODUCTION

Single-molecule localization microscopy (SMLM) is a super-resolved fluorescence imaging technique based on precise localization of fluorophores [1]. Because the lateral resolution is inversely proportional to the numerical aperture (NA), this technique employs high-NA objectives, which considerably limits its natural depth-of-field (DoF). Several groups have demonstrated that placing a phase mask in the aperture stop of a localization microscope can significantly increase its DoF [2–5]. Recently, we have proposed to use annular binary phase masks to extend 2D localization performance within a prescribed DoF range [6,7] (see Fig. 1). These masks are optimized using a criterion based on the Cramér–Rao bound (CRB), which is a lower bound on localization variance [8]. We have shown that an adapted maximum likelihood estimator (MLE) for 2D localization estimation is able to reach this bound in practice, but this demonstration was done under particular conditions: pure additive noise model, large values of the signal-to-noise ratio (SNR), and a given microscope configuration [7].

A question therefore arises: if one deviates from this particular configuration, is it still possible to reach the CRB using an MLE? The performance of the MLE has already been quantified in different scenarios in the case of focused SMLM methods [9], and it is widely believed that it can always attain the CRB in practice [10,11]. However, classical signal processing theory says that if the SNR becomes too small, the variance of the MLE is worse than the CRB [8]. The purpose of this paper is thus to

precisely delineate the domain in which MLE-based enhanced DoF (EDoF) SMLM methods effectively reach the CRB, by exploring a wide range of settings and noise levels.

The paper is organized as follows. In Section 2, we define the image formation models considered in the paper and review the

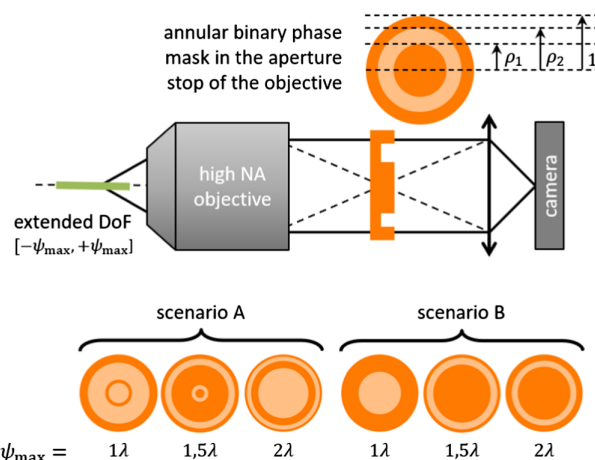


Fig. 1. EDoF localization microscopy setup: an optimized phase mask is placed in the aperture stop of the microscope objective. We consider in this paper six annular binary phase masks, respectively, optimized for $\psi_{\max} = \{1\lambda, 1.5\lambda, 2\lambda\}$ in *Scenarios A* and *B*. This type of mask is based on concentric rings implementing static spatial phase modulations of alternatively 0 and π radians at a nominal wavelength λ .

corresponding expressions of the CRB. In Section 3, we develop our methodology and apply it to delineate the domain in which the MLE is efficient (i.e., reaches the CRB) for standard in-focus SMLM methods. In Section 4, we apply this methodology to investigate the domain of efficiency of the MLE-based SMLM methods with EDoF that use binary annular phase masks. Section 5 is devoted to concluding remarks and perspectives.

2. IMAGE FORMATION AND LOCALIZATION ACCURACY

Consider an emitter located at an axial distance Δz_p from the focus plane and at a lateral position $\boldsymbol{\theta} = (x_p, y_p)$. Our goal is to optimize the estimation of $\boldsymbol{\theta}$ over a certain range of defocus distances Δz_p . Assuming that the image formation process is space invariant, the image of this emitter is proportional to the normalized 2D spatial irradiance of the point spread function (PSF) of the microscope objective centered on $\boldsymbol{\theta}$:

$$f^\theta(x, y) \propto$$

$$\left| \int_0^1 J_0 \left(\frac{2\pi}{\lambda} \sqrt{\left(\frac{x}{M} - x_p\right)^2 + \left(\frac{y}{M} - y_p\right)^2} \text{NA}r \right) e^{i\Phi(r)} r dr \right|^2, \quad (1)$$

and $\iint f^\theta(x, y) dx dy = 1$. In Eq. (1), $J_0(\cdot)$ is the Bessel function of the first kind of order zero, λ is the wavelength of the collected light, M is the lateral magnification, NA is the object numerical aperture, and $\Phi(r)$ is the pupil phase function that depends on Δz_p and on the possible presence of a phase mask. In the case of well focused emitters with no phase mask and no optical aberration, $\Phi(r) = 0$, and the 2D spatial distribution of collected fluorescence is the Airy pattern. Note that the formalism defined in Eq. (1) is limited to phase functions $\Phi(r)$ having circular symmetry, since the annular binary phase masks that we use in the following have this symmetry. However, the methodology of this paper can easily be extended to the many non-circularly symmetric DoF-extending phase masks proposed in the literature, see, e.g., [12–17].

The image of the PSF is acquired by an array sensor and corrupted by noise. According to [18], the dominant sources of corruption in SMLM are shot noise arising from the useful fluorescence signal (i.e., the emitter) and from the fluorescent background (e.g., from the autofluorescence of the biological environment). In consequence, we shall consider only these two types of noise sources in this paper.

Let us denote by s_{ij} the data acquired at pixel (i, j) over a square region $(2P + 1) \times (2P + 1)$, so that $(i, j) \in \{-P, \dots, P\}^2$. It is modeled as a Poisson random variable of mean $N_0 r_{ij}(\boldsymbol{\theta}) + b$, where N_0 is the total number of photo-electrons expected in the whole image from the emitter, $r_{ij}(\boldsymbol{\theta})$ is the value of the PSF integrated over the square pixel (i, j) of side length Δ_{xy} :

$$r_{ij}(\boldsymbol{\theta}) = \int_{(i-\frac{1}{2})\Delta_{xy}}^{(i+\frac{1}{2})\Delta_{xy}} \int_{(j-\frac{1}{2})\Delta_{xy}}^{(j+\frac{1}{2})\Delta_{xy}} f^\theta(x, y) dx dy, \quad (2)$$

and b is the spatially constant mean value of the background per pixel. The value of b depends on the application, and, for the

sake of simplicity, we consider in this paper the two following extreme scenarios. In *Scenario A*, we consider only the shot noise due to the light of the fluorescent emitter, i.e., we assume that $b = 0$. In *Scenario B*, we consider that the autofluorescent background is the dominant source of noise, i.e., we neglect the fluctuations due to the signal from the emitter, which leads to $N_0 r_{ij}(\boldsymbol{\theta}) \ll b$. Realistic background noise levels therefore lie between these two extreme scenarios.

Our goal is to estimate the fluorophore lateral position $\boldsymbol{\theta}$ from the measured data s_{ij} . Since this data is noisy, so is the position estimate, and a lower bound on the variance of the estimation is given by the CRB. The square root of the CRB, denoted as **RCRB** = (RCRB_x, RCRB_y), has the following expressions along the x and y axes:

$$\text{RCRB}_x = \left[\sum_{i=-P}^P \sum_{j=-P}^P \frac{N_0^2 \left(\int_{(j-\frac{1}{2})\Delta_{xy}}^{(j+\frac{1}{2})\Delta_{xy}} \Delta_x f_i^{\theta_0}(y) dy \right)^2}{N_0 r_{ij}(\boldsymbol{\theta}_0) + b} \right]^{-\frac{1}{2}}, \quad (3)$$

$$\text{RCRB}_y = \left[\sum_{i=-P}^P \sum_{j=-P}^P \frac{N_0^2 \left(\int_{(i-\frac{1}{2})\Delta_{xy}}^{(i+\frac{1}{2})\Delta_{xy}} \Delta_y f_j^{\theta_0}(x) dx \right)^2}{N_0 r_{ij}(\boldsymbol{\theta}_0) + b} \right]^{-\frac{1}{2}}, \quad (4)$$

where $\Delta_x f_i^{\theta_0}(y)$ (respectively, $\Delta_y f_j^{\theta_0}(x)$) is the difference between the PSF samples at the edge of the pixels of row i (respectively, column j), i.e.,

$$\begin{aligned} \Delta_x f_i^{\theta_0}(y) &= f^{\theta_0} \left(\left[i - \frac{1}{2} \right] \Delta_{xy}, y \right) \\ &\quad - f^{\theta_0} \left(\left[i + \frac{1}{2} \right] \Delta_{xy}, y \right), \end{aligned} \quad (5)$$

$$\begin{aligned} \Delta_y f_j^{\theta_0}(x) &= f^{\theta_0} \left(x, \left[j - \frac{1}{2} \right] \Delta_{xy} \right) \\ &\quad - f^{\theta_0} \left(x, \left[j + \frac{1}{2} \right] \Delta_{xy} \right). \end{aligned} \quad (6)$$

The values of the RCRB in Eqs. (3) and (4) depend on the actual position $\boldsymbol{\theta}_0$ of the PSF with respect to the pixel grid [6]. In this paper, we shall consider the two following extreme cases. In the first one, the PSF is located at the center of a pixel [e.g., $\boldsymbol{\theta}_0 = (0, 0)$]. This position corresponds to the largest possible value of the CRB, i.e., the worst case for localization accuracy [7]. In the second case, the PSF is centered on the corner of a pixel, e.g., $\boldsymbol{\theta}_0 = (\Delta_{xy}/2, \Delta_{xy}/2)$. This position corresponds to the smallest possible value of the CRB, i.e., the most favorable case for localization accuracy. Note that in these two cases $\text{RCRB}_x = \text{RCRB}_y$.

The RCRB expressions given in Eqs. (3) and (4) are a version of those given in Ref. [6] for pure signal-based shot noise but generalized to take into account a constant background noise of mean level b . In *Scenario A*, where the background noise is neglected, the expressions of the RCRB are easily obtained by

setting $b = 0$ in Eqs. (3) and (4). In *Scenario B*, where the fluctuations of the useful signal are neglected, we have $N_0 r_{ij}(\boldsymbol{\theta}) \ll b$, so the expressions of the RCRB can be approximated by

$$\text{RCRB}_x = \frac{\sqrt{b}}{N_0} \left[\sum_{i=-P}^P \sum_{j=-P}^P \left(\int_{(j-\frac{1}{2})\Delta_{xy}}^{(j+\frac{1}{2})\Delta_{xy}} \Delta_x f_i^{\theta_0}(y) dy \right)^2 \right]^{-\frac{1}{2}}, \quad (7)$$

$$\text{RCRB}_y = \frac{\sqrt{b}}{N_0} \left[\sum_{i=-P}^P \sum_{j=-P}^P \left(\int_{(i-\frac{1}{2})\Delta_{xy}}^{(i+\frac{1}{2})\Delta_{xy}} \Delta_y f_j^{\theta_0}(x) dx \right)^2 \right]^{-\frac{1}{2}}. \quad (8)$$

Note that these expressions, which relate to additive Poisson noise, are the same as those of the RCRB for additive Gaussian noise with variance $\sigma^2 = b$, see, e.g., Ref. [7].

3. VALIDITY DOMAIN OF STANDARD SMLM METHODS

To estimate the emitter position with subpixel precision, a localization algorithm needs to be implemented. For that purpose, different methods based on center of mass estimation, template fitting, or deconvolution with sparsity constraints have been proposed [19]. However, a commonly employed algorithm is the MLE, whose advantage is to leverage our knowledge about the nature of the noise sources that corrupt the observed images [10]. For a Poisson noise model, the MLE has the following expression:

$$\hat{\boldsymbol{\theta}} = \arg \max_{\boldsymbol{\theta}} \left\{ \sum_{i=-P}^P \sum_{j=-P}^P s_{ij} q_{ij}(\boldsymbol{\theta}) \right\}, \quad (9)$$

where

$$q_{ij}(\boldsymbol{\theta}) = \log [N_0 r_{ij}(\boldsymbol{\theta}) + b]. \quad (10)$$

It is interesting to note that in *Scenario A*, q_{ij} is proportional to $\log[r_{ij}(\boldsymbol{\theta})]$, and, in *Scenario B*, it is quasi-proportional to $r_{ij}(\boldsymbol{\theta})$ since, in this case, $\log[1 + N_0 r_{ij}(\boldsymbol{\theta})/b] \simeq N_0 r_{ij}(\boldsymbol{\theta})/b$. Thus, in *Scenario B*, although the noise is Poisson distributed, the expression of the MLE can be approximated by the matched filter, which is optimal in the presence of additive Gaussian noise [8].

In the case of emitters located in the focusing plane, it has been shown that for good SNR, the MLE is unbiased and able to reach the CRB [10]. In order to precisely delineate the domain of validity of this assertion, let us assume that the observed emitter is centered on a pixel with $\boldsymbol{\theta}_0 = (0, 0)$ (the least favorable case for localization accuracy). In this configuration, the value of the RCRB is equal in the x and y directions, and we shall denote it as $\text{RCRB} = \text{RCRB}_x = \text{RCRB}_y$. Obviously, the bias ($E[\hat{\boldsymbol{\theta}}] - \boldsymbol{\theta}_0$, where $E[\cdot]$ denotes the mathematical expectation operation, and $\boldsymbol{\theta}_0$ is the true position of the emitter) and the standard deviation $\text{STD}[\hat{\boldsymbol{\theta}}]$ of the MLE are also equal in the x and y directions. To delineate the domain of validity of the MLE, we will study the normalized versions of these values, namely,

$$\text{nBias} = \frac{E[\hat{\boldsymbol{\theta}}] - \boldsymbol{\theta}_0}{\text{RCRB}} \quad \text{and} \quad \text{nSTD} = \frac{\text{STD}[\hat{\boldsymbol{\theta}}]}{\text{RCRB}}. \quad (11)$$

These values are estimated with Monte-Carlo simulations on 4000 noise realizations. We have checked that this number of Monte-Carlo realizations are sufficient: using more realizations does not change the results.

The values of normalized bias (nBias) are represented in Fig. 2(a), and those of normalized standard deviation (nSTD) in Fig. 2(b), for *Scenario A* (black dot markers) and *Scenario B* (red cross markers). These values are plotted as a function of the RCRB. This means that large SNR values correspond to the left side of the curve, and SNR decreases as one goes to the right. In this representation, if the MLE is efficient, the nBias should be close to zero and the nSTD close to one. The optical parameters considered in this simulation are typical of standard SMLM setups: $\Delta_{xy} = 10 \mu\text{m}$, $\text{NA} = 1.3$, $\lambda = 700 \text{ nm}$, and $M = 60$ (magnification). In the simulations, the increasing values of RCRB are obtained by reducing the SNR, whose expression depends on the scenario. In *Scenario A*, the SNR is defined as $\sqrt{N_0}$ [see Eq. (3) when $b = 0$] and is varied in the range 75 to 99 to cover the desired values of the RCRB. In *Scenario B*, it is defined as N_0/\sqrt{b} [see Eq. (7)] and is varied in the range 303 to 4.4. Note that representing the bias and the standard deviation as a function of the RCRB instead of the SNR has the advantage of making it possible to visualize the two types of noise configurations on the same graph.

We observe on Fig. 2(a) that for both *Scenarios A* and *B*, the bias is close to zero, and the nSTD is close to one as long as $\text{RCRB} \leq 20\text{--}30 \text{ nm}$. In this range of RCRB values, the MLE is thus efficient. Then, when $\text{RCRB} > 30 \text{ nm}$, the standard deviation starts to diverge, while the bias remains close to zero before diverging in turn when $\text{RCRB} > 40 \text{ nm}$. In order to check that these conclusions remain the same if $\boldsymbol{\theta}_0$ is not centered on a pixel, we have also considered the case where the actual PSF position $\boldsymbol{\theta}_0$ is at the corner of a pixel, with $\boldsymbol{\theta}_0 = (\Delta_{xy}/2, \Delta_{xy}/2)$. In this case also, the symmetry of the problem is such that the

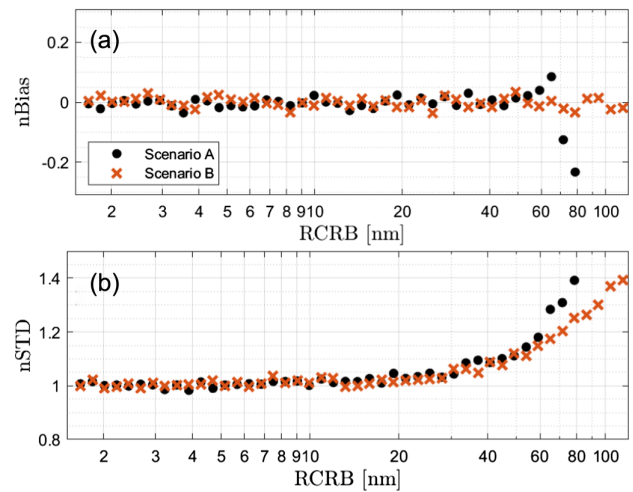


Fig. 2. Estimation properties of the MLE when the fluorescent emitter is in-focus and at the center of a pixel for (a) the normalized bias (nBias) and (b) the normalized standard deviation (nSTD), as a function of the RCRB for *Scenarios A* (black dots) and *B* (red crosses). The simulation parameters are $\boldsymbol{\theta}_0 = (0, 0) \mu\text{m}$, $\Delta_{xy} = 10 \mu\text{m}$, $2P + 1 = 21$ pixels, $\text{NA} = 1.3$, $\lambda = 700 \text{ nm}$, $M = 60$ (magnification).

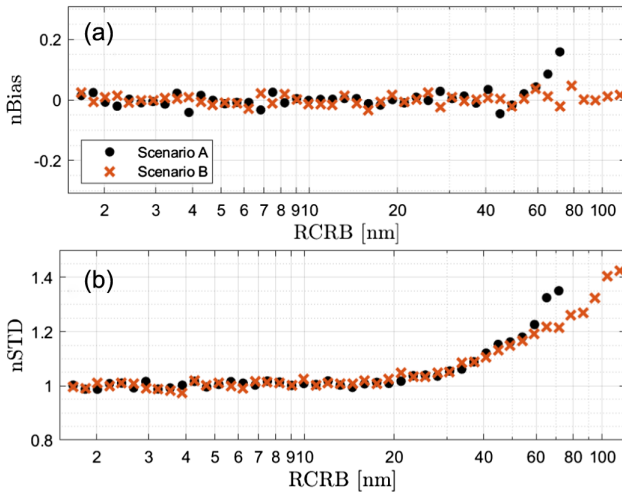


Fig. 3. Estimation properties of the MLE when the fluorescent emitter is in-focus and at the corner of a pixel for (a) the nBias and (b) the nSTD, as a function of the RCRB for *Scenario A* (black dots) and *B* (red crosses). The simulation parameters are given in Fig. 2 except for $\theta_0 = (5, 5) \mu\text{m}$.

bias, the standard deviation, and the RCRB have the same value along the x and y axes. We have represented in Fig. 3 the values of nBias and nSTD for this configuration. The noise realizations are not the same as those used in Fig. 2. We can see that the graphs are very similar to those in Fig. 2. In particular, the MLE is efficient for RCRB < 20 nm. This conclusion is thus independent of the PSF position.

As a summary, in low SNR conditions, the actual localization accuracy is worse than the one predicted by the CRB. Fortunately, this problem does not affect cases of higher SNR: for the standard experimental parameters that we have assumed, the MLE remains efficient as long as the RCRB is smaller than 20 nm. Care should thus be taken when experiments are conducted in low SNR conditions since the standard deviation of the MLE does not reach the RCRB in this case.

As an aside, we can note that an advantage of representing the bias and the standard deviation as a function of the RCRB in Figs. 2 and 3 is that this type of graph can be used as an abacus. Indeed, in a given application, whatever the type of noise, the SNR, and other optical parameters, the RCRB can be computed. If the RCRB is lower than 20 nm, it can be safely considered as a correct evaluation of the precision that can be reached in practice with the MLE. If it is larger, this is no longer the case.

4. VALIDITY DOMAIN OF MLE-BASED EDFOF SMLM METHODS

Let us now consider the case of emitters with axial positions distant from the imaging plane: they are out-of-focus. To quantify this defocus, we use the standard parameter ψ , which is the wavefront error at the edge of the pupil [20]:

$$\psi = \frac{\text{NA}^2 \Delta z_p}{2n}, \quad (12)$$

where Δz_p is the axial distance between the observed emitter and the focus point, and n is the refractive index of the object space. Naturally, the expression of the PSF, and thus of the RCRB, now depends on the defocus parameter ψ through the pupil phase function:

$$\Phi(r) = \frac{2\pi}{\lambda} \psi r^2 + \Phi_{\text{mask}}(r), \quad (13)$$

where $\Phi_{\text{mask}}(r)$ is the phase function of a mask possibly added in the optical path.

Without a mask, the localization precision degrades as ψ increases. We have shown in Ref. [6] that placing an optimized annular binary phase mask in the aperture stop of the microscope allows us to significantly increase the localization performance within a required DoF range by reducing the spread of the PSF due to defocus. The optimal mask is entirely characterized by the vector $\rho_{\text{opt}} = (\rho_1, \rho_2, \dots, \rho_{L-1})$ of the normalized radii of each ring (the last radius is at the edge of the aperture, i.e., $\rho_L = 1$), such as

$$\rho_{\text{opt}} = \arg \min_{\rho} \left\{ \max_{\psi \in [-\psi_{\text{max}}, \psi_{\text{max}}]} \text{RCRB}(\rho, \psi) \right\}. \quad (14)$$

Note that the expression of the RCRB is different in *Scenario A* [see Eqs. (3) and (4) with $b = 0$] and *Scenario B* [see Eqs. (7) and (8)]. Hence, the optimal masks in these two scenarios will be different, even for the same targeted defocus range ψ_{max} . We also notice that in these two scenarios, the SNR appears as a simple multiplying factor in the expression of the RCRB. The optimized masks are therefore independent of the SNR. This approach was presented in detail for a pure additive Gaussian noise model in [7], and it was shown that even with an optimal mask the PSF shape still significantly varies with defocus. To reach the RCRB, it is thus necessary to use an approximate MLE, which consists in dividing the DoF range into a finite number of sub-ranges in order to define a reference kernel adapted to each sub-range.

Suppose that the targeted DoF range $[0, \psi_{\text{max}}]$ is split into M_ψ distinct sub-ranges. Note that this is equivalent to the interval $[-\psi_{\text{max}}, \psi_{\text{max}}]$ since, independently of the presence or absence of the annular binary mask with a π modulation, the PSF is identical for ψ and $-\psi$ (i.e., on either side of the focus point) [7]. To each DoF sub-range, we can associate a unique kernel, denoted by $r_{ij}^m(\theta)$, with $m \in \{1, \dots, M_\psi\}$. This kernel is built as a linear combination of characteristic PSFs in this sub-range:

$$r_{ij}^m(\theta) = \sum_{k=1}^K \alpha_k r_{ij}(\theta), \quad (15)$$

where the coefficients α_k are the components of the eigenvector associated with the greatest eigenvalue of the matrix \underline{W} defined as

$$[\underline{W}]_{ij} = \iint_{\mathbb{R}^2} v_x v_y \tilde{f}^*(v_x, v_y, \psi_i) \tilde{f}(v_x, v_y, \psi_j) dv_x dv_y, \quad (16)$$

with $\tilde{f}(v_x, v_y, \psi)$ the Fourier transform of $f^\theta(x, y)$ defined in Eq. (1). The dependence on ψ is made explicit, and the superscript $*$ denotes the complex conjugate. The proof of Eq. (16)

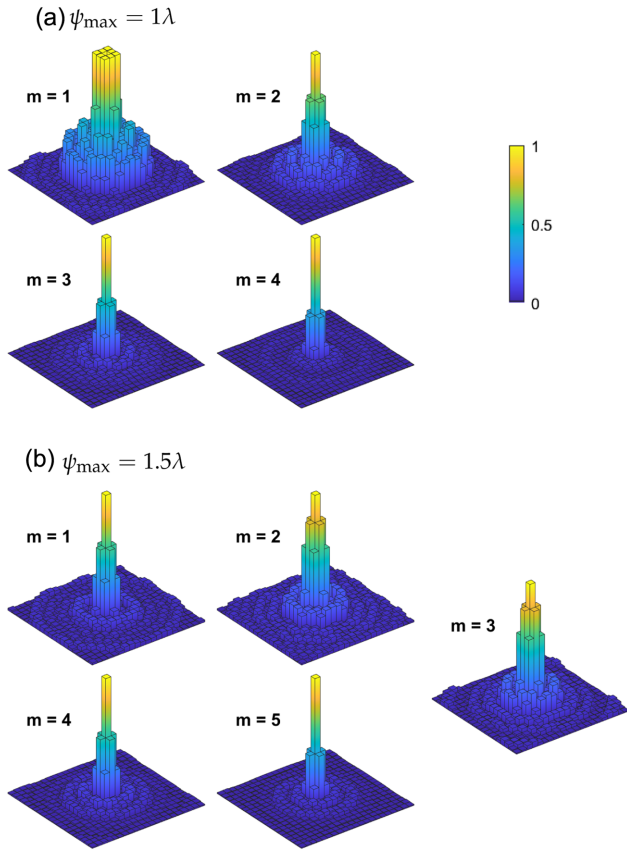


Fig. 4. Average PSF kernels $r_{ij}^m(\theta)$ defined in Eq. (15) and used in the approximate MLE of Fig. 5 (*Scenario A*) when (a) $\psi_{\max} = 1\lambda$ or (b) $\psi_{\max} = 1.5\lambda$.

is described in [7]. For example, let us assume that the targeted DoF range is $\psi_{\max} = 1\lambda$ in *Scenario A*. In this case, the MLE requires $M_\psi = 4$ DoF sub-ranges, and m can thus take four different values: $[0, 0.2\lambda]$ ($m = 1$), $[0.2\lambda, 0.35\lambda]$ ($m = 2$), $[0.35\lambda, 0.5\lambda]$ ($m = 3$), and $[0.5\lambda, 1\lambda]$ ($m = 4$), as shown in [6]. The associated kernels $r_{ij}^m(\theta)$, with $m \in \{1, \dots, 4\}$, are illustrated in Fig. 4(a). The number M_ψ of DoF sub-ranges depends on the value of the targeted DoF range ψ_{\max} and on the scenario. We have illustrated, in Fig. 4(b), the five kernels $r_{ij}^m(\theta)$ that are needed when $\psi_{\max} = 1.5\lambda$ in *Scenario A*.

This estimator thus requires joint estimation of the emitter position θ and of the defocus sub-range m in which it is located:

$$(\hat{\theta}, \hat{m}) = \arg \max_{\theta, m} \left\{ \sum_{i=-P}^P \sum_{j=-P}^P s_{ij} q_{ij}^m(\theta) \right\}, \quad (17)$$

with $q_{ij}^m(\theta) = \log[r_{ij}^m(\theta)]$ in *Scenario A* and $q_{ij}^m(\theta) = r_{ij}^m(\theta)$ in *Scenario B*. Note that in this paper, our goal is 2D localization estimation with EDoF, so that our masks are not optimized to retrieve the 3D localization of the emitters. Our only parameter of interest in this study therefore remains the lateral position θ . However, to estimate it, estimation of the nuisance parameter ψ is necessary. We have shown in [7] that a crude estimation of ψ using a limited number M_ψ of kernels [see Eq. (17)] was sufficient to yield acceptable results in practice. The (modest) price to pay on localization performance for this approximation will

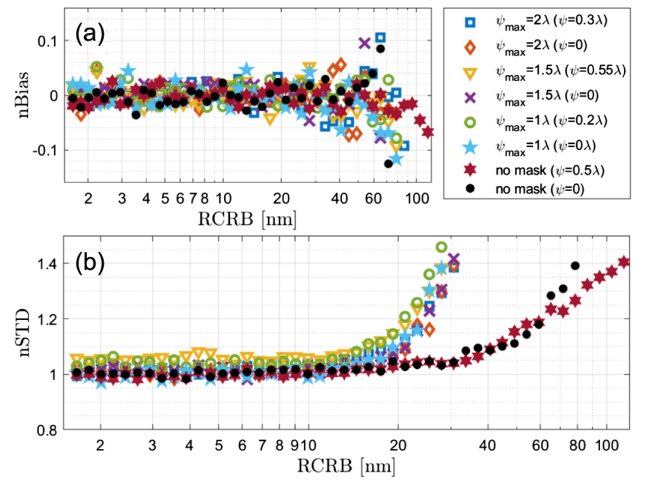


Fig. 5. Estimation properties, (a) the bias and (b) the standard deviation, of the approximate MLE designed for EDoF in *Scenario A*, with $\psi_{\max} = \{1\lambda, 1.5\lambda, 2\lambda\}$, as a function of the RCRB for in-focus emitters (i.e., $\psi = 0$) and out-of-focus emitters (i.e., $\psi \neq 0$). The simulation parameters are given in Fig. 2.

be discussed at the end of the section. Moreover, since the kernels $r_{ij}^m(\theta)$ are not actual PSFs, the estimator defined in Eq. (17) is not strictly speaking as an MLE. However, we use this term in the following for the sake of simplicity, as this algorithm is able to reach the CRB in the presence of pure additive Gaussian noise and for high enough SNR [7]. Our goal hereafter is to fully characterize its domain of validity, i.e., the range of RCRB values for which it actually reaches the localization performance predicted by the RCRB. Note that the gain in absolute localization performance (or absolute RCRB) obtained by using a mask has already been evaluated previously in detail [6,7].

Let us consider several previously determined annular binary phase masks with π modulation that optimize the RCRB in *Scenario A* [6] and *Scenario B* [7], for various targeted DoF ranges $\psi_{\max} = \{1\lambda, 1.5\lambda, 2\lambda\}$. These phase masks are illustrated and described in Fig. 1. For all of these DoF ranges, we have represented the bias of the MLE in *Scenario A* [see Fig. 5(a)] and in *Scenario B* [see Fig. 6(a)] as a function of the RCRB for two different values of the defocus parameter ψ . In addition, we have represented the standard deviation of the MLE in *Scenario A* [see Fig. 5(b)] and in *Scenario B* [see Fig. 6(b)]. As references, we have added to these two figures the curves obtained without phase mask for an in-focus emitter ($\psi = 0$), that were also displayed in Fig. 2, and for an out-of-focus emitter ($\psi = 0.5\lambda$) when θ_0 is estimated with Eq. (9). We observe that for all the considered DoF ranges ψ_{\max} , the MLE is unbiased, and its standard deviation reaches the RCRB when $\text{RCRB} \leq 20\text{nm}$. The main conclusion of these graphs is therefore that the domain in which the MLE reaches the RCRB is comparable for mask-less and EDoF setups, even though in the latter case, the implementation of the MLE is more complex since it requires joint estimation of the lateral position and of the DoF sub-range [see Eq. (17)].

In order to understand more precisely how the statistical distribution of the position estimates changes when the RCRB gets larger than 20 nm, we have plotted in Fig. 7 the evolution of the histogram of $(E[\hat{\theta}] - \theta_0)/\text{RCRB}$ (with

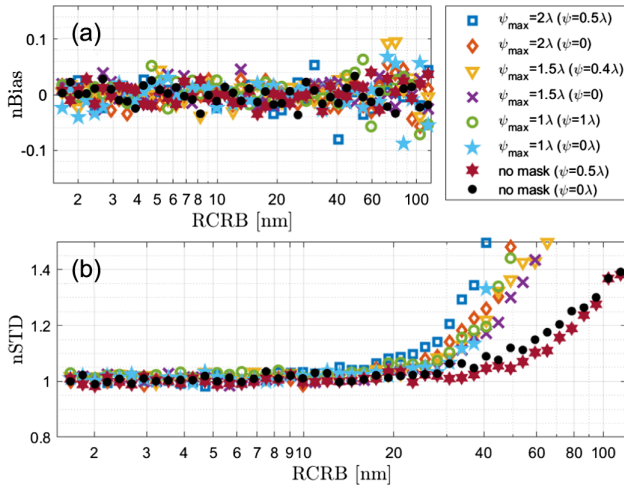


Fig. 6. Estimation properties, (a) the bias and (b) the standard deviation, of the approximate MLE designed for EDoF in *Scenario B*, with $\psi_{\max} = \{1\lambda, 1.5\lambda, 2\lambda\}$, as a function of the RCRB for in-focus emitters (i.e., $\psi = 0$) and out-of-focus emitters (i.e., $\psi \neq 0$). The simulation parameters are given in Fig. 2.

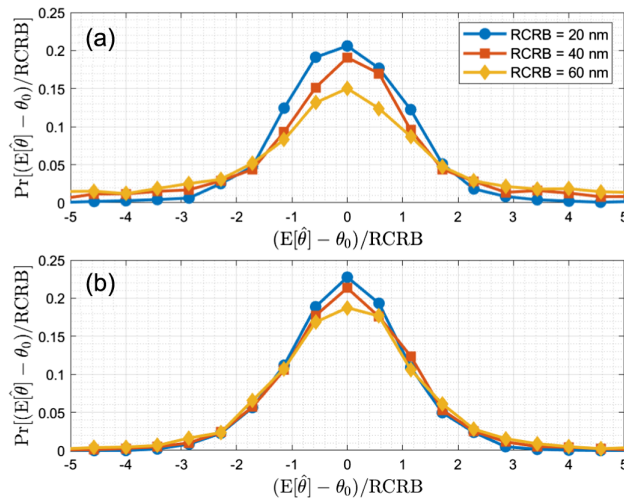


Fig. 7. Histograms of $(E[\hat{\theta}] - \theta_0)/RCRB$ as a function of the RCRB when (a) $\psi_{\max} = 1\lambda$, $\psi = 0.2\lambda$ in *Scenario A* and (b) $\psi_{\max} = 1.5\lambda$, $\psi = 0.4\lambda$ in *Scenario B*. The simulation parameters are given in Fig. 2.

$RCRB = RCRB_x = RCRB_y$) as a function of the RCRB in two examples of configurations. We observe that the histograms widen progressively with decreasing SNRs. The increase of variance is thus not due to the presence of some isolated bad outliers.

Analyzing in more detail the results in Figs. 5(b) and 6(b), we can notice two interesting points. First, for some values of the DoF range ψ_{\max} and of the defocus parameter ψ , the localization performance is not exactly equal to the RCRB even when $RCRB < 20\text{nm}$: one can notice that some standard deviation curves are slightly larger than one, by a factor up to 5%. Second, when the RCRB gets larger than 20 nm, the localization performance deviates from the RCRB much faster in the presence of a phase mask, compared with the curves obtained without phase mask (black dots and purple stars).

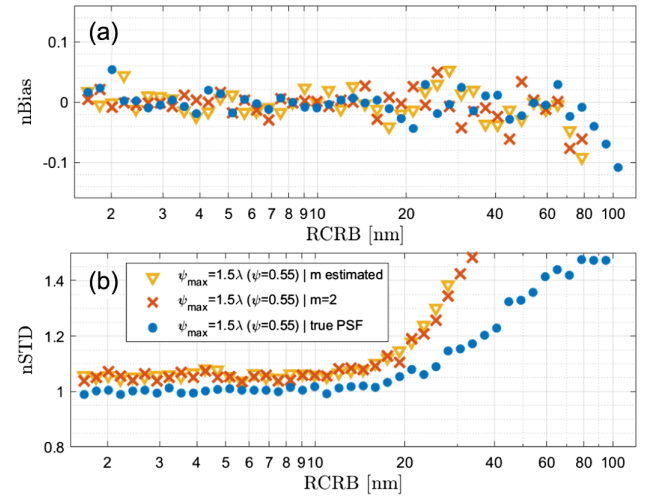


Fig. 8. Estimation property comparison, for $\psi_{\max} = 1.5\lambda$ and $\psi = 0.55\lambda$, of (a) the bias and (b) the standard deviation obtained with the MLE defined in Eq. (17). This approximate MLE requires either the joint estimation of the correct matched kernels (yellow triangular markers), a hand selection (red cross markers), or the use of the true PSF (blue circular markers). The simulation parameters are given in Fig. 2.

To explain these two observations, we compare in Fig. 8, for a given configuration (namely, $\psi_{\max} = 1.5\lambda$ and $\psi = 0.55\lambda$), the values of nBias and nSTD obtained with three different ML-based localization algorithms as a function of RCRB. The first algorithm is the approximate MLE defined in Eq. (17) (curve with yellow triangular markers). In the second case, we assume to know the true defocus range $m_0 = 2$ in which the emitter lies and apply the MLE defined in Eq. (9) with reference kernel $r_{ij} = r_{ij}^{m_0}$ (red cross markers). In the third case, one uses the MLE defined in Eq. (9) with the reference kernel r_{ij} equal to the true PSF of the configuration $\psi_{\max} = 1.5\lambda$ and $\psi = 0.55\lambda$ (blue circular markers). We observe that the curves obtained with the first and second algorithm are similar, having a standard deviation slightly larger than one for $RCRB < 20\text{nm}$ and a fast increase after $RCRB > 20\text{nm}$. This means that the estimation of the defocus range m in the approximate MLE defined in Eq. (17) is correct, since assuming to know *a priori* the correct kernel does not improve the performance. In contrast, the curve obtained with the third algorithm is very close to one when $RCRB < 20\text{nm}$ and has a much slower increase, similar to what is observed in the focused case. This means that the slight discrepancy in the standard deviation observed in some cases for $RCRB < 20\text{nm}$ and its sharper increase when RCRB gets larger than 20 nm comes from the mismatch between the average PSF kernel used in the localization algorithm of Eq. (17) and the real PSF. This mismatch could be reduced by increasing the number M_ψ of defocus subranges considered in Eq. (17). The cost of the calculations would grow linearly with M_ψ .

Note that, in practice, other factors such as optical aberrations or inaccurate PSF calibration can further increase the mismatch between the actual PSF and the correlation kernel. For example, several recent works have investigated the sensitivity of localization algorithms based on PSF fitting [21–23] to a mismatch between actual and calibrated PSF.

5. CONCLUSION

In conclusion, we have delineated the domain in which the CRB is able to accurately predict the localization precision of SMLM experiments. We have shown that the MLE is efficient (i.e., unbiased and reaching the RCRB) when the experiment parameters are such that the RCRB is less than 20 nm. This limit is identical for standard and EDoF setups, but, in the latter case, the divergence of the MLE performance beyond this limit is much faster. We also observed that EDoF setups may have a standard deviation slightly larger than the RCRB when $\text{RCRB} < 20$ nm. This comes from the mismatch between the actual PSF and the correlation kernel used in the localization algorithm. Since many SMLM experiments are conducted in conditions where $\text{RCRB} < 20$ nm, the common practice of evaluating or optimizing setups using the CRB and employing the MLE to reach the predicted performance is most often valid. However, when experimental conditions are such that $\text{RCRB} > 20$ nm, care has to be taken as the CRB no longer faithfully represents the MLE performance in low SNR scenarios.

An interesting perspective of this work is to apply the developed methodology to precisely delineate the domain of efficiency of 3D localization setups [2–4].

Funding. Agence Nationale de la Recherche (ANR) (ANR-18-CE09-0019-02); Fondation ARC pour la Recherche sur le Cancer; French research group GdR ISIS of the CNRS.

Acknowledgment. A. L. acknowledges support from ANR and the Fondation ARC pour la Recherche sur le Cancer.

Disclosures. The authors declare no conflicts of interest.

Data Availability. Data underlying the results presented in this paper are not publicly available at this time but may be obtained from the authors upon reasonable request.

REFERENCES

1. A. G. Godin, B. Lounis, and L. Cognet, "Super-resolution microscopy approaches for live cell imaging," *Biophys. J.* **107**, 1777–1784 (2014).
2. S. R. P. Pavani and R. Piestun, "Three dimensional tracking of fluorescent microparticles using a photon-limited double-helix response system," *Opt. Express* **16**, 22048–22057 (2008).
3. Y. Shechtman, S. J. Sahl, A. S. Backer, and W. E. Moerner, "Optimal point spread function design for 3D imaging," *Phys. Rev. Lett.* **113**, 133902 (2014).
4. Y. Zhou and G. Carles, "Precise 3D particle localization over large axial ranges using secondary astigmatism," *Opt. Lett.* **45**, 2466–2469 (2020).
5. J. Ren and K. Y. Han, "2.5D microscopy: fast, high-throughput imaging via volumetric projection for quantitative subcellular analysis," *ACS Photon.* **8**, 933–942 (2021).
6. O. Lévêque, C. Kulcsár, H. Sauer, A. Lee, P. Bon, L. Cognet, and F. Goudail, "Can phase masks extend depth-of-field in localization microscopy?" *Proc. SPIE* **11351**, 113510E (2020).
7. O. Lévêque, C. Kulcsár, A. Lee, H. Sauer, A. Aleksanyan, P. Bon, L. Cognet, and F. Goudail, "Co-designed annular binary phase masks for depth-of-field extension in single-molecule localization microscopy," *Opt. Express* **28**, 32426–32446 (2020).
8. S. M. Kay, *Fundamentals of Statistical Signal Processing: Estimation Theory*, Prentice Hall Signal Processing Series (Prentice-Hall PTR, 1993).
9. A. V. Abraham, S. Ram, J. Chao, E. S. Ward, and R. J. Ober, "Quantitative study of single molecule location estimation techniques," *Opt. Express* **17**, 23352–23373 (2009).
10. R. J. Ober, S. Ram, and E. S. Ward, "Localization accuracy in single-molecule microscopy," *Biophys. J.* **86**, 1185–1200 (2004).
11. B. Rieger and S. Stallinga, "The lateral and axial localization uncertainty in super-resolution light microscopy," *ChemPhysChem* **15**, 664–670 (2014).
12. E. R. Dowski and W. T. Cathey, "Extended depth of field through wave-front coding," *Appl. Opt.* **34**, 1859–1866 (1995).
13. S. S. Sherif, W. T. Cathey, and E. R. Dowski, "Phase plate to extend the depth of field of incoherent hybrid imaging systems," *Appl. Opt.* **43**, 2709–2721 (2004).
14. A. Saucedo and J. Ojeda-Castañeda, "High focal depth with fractional-power wave fronts," *Opt. Lett.* **29**, 560–562 (2004).
15. Q. Yang, L. Liu, and J. Sun, "Optimized phase pupil masks for extended depth of field," *Opt. Commun.* **272**, 56–66 (2007).
16. N. Caron and Y. Sheng, "Polynomial phase masks for extending the depth of field of a microscope," *Appl. Opt.* **47**, E39–E43 (2008).
17. F. Zhou, G. Li, H. Zhang, and D. Wang, "Rational phase mask to extend the depth of field in optical-digital hybrid imaging systems," *Opt. Lett.* **34**, 380–382 (2009).
18. F. Aguet, D. V. D. Ville, and M. Unser, "A maximum-likelihood formalism for sub-resolution axial localization of fluorescent nanoparticles," *Opt. Express* **13**, 10503–10522 (2005).
19. D. Sage, T.-A. Pham, H. Babcock, T. Lukes, T. Pengo, J. Chao, R. Velmurugan, A. Herbert, A. Agrawal, S. Colabrese, A. Wheeler, A. Archetti, B. Rieger, R. Ober, G. M. Hagen, J.-B. Sibarita, J. Ries, R. Henriques, M. Unser, and S. Holden, "Super-resolution fight club: assessment of 2D and 3D single-molecule localization microscopy software," *Nat. Methods* **16**, 387–395 (2019).
20. J. W. Goodman, *Introduction to Fourier Optics*, 4th ed. (Freeman, 2017).
21. R. Ø. Thorsen, C. N. Hulleman, M. Hammer, D. Grünwald, S. Stallinga, and B. Rieger, "Impact of optical aberrations on axial position determination by photometry," *Nat. Methods* **15**, 989–990 (2018).
22. M. Siemons, C. N. Hulleman, R. Ø. Thorsen, C. S. Smith, and S. Stallinga, "High precision wavefront control in point spread function engineering for single emitter localization," *Opt. Express* **26**, 8397–8416 (2018).
23. H. Mazidi, T. Ding, A. Nehorai, and M. D. Lew, "Quantifying accuracy and heterogeneity in single-molecule super-resolution microscopy," *Nat. Commun.* **11**, 6353 (2020).